

Comparison of cavities and extended defects formed in helium-implanted 6H-SiC at room temperature and 750 ℃

Qing Liao(廖庆), Bingsheng Li(李炳生), Long Kang(康龙), Xiaogang Li(李小刚)

Citation: Chin. Phys. B . 2020, 29(7): 076103 . **doi:** 10.1088/1674-1056/ab8abc
Journal homepage: http://cpb.iphy.ac.cn; http://iopscience.iop.org/cpb

What follows is a list of articles you may be interested in

Defects and electrical properties in Al-implanted 4H-SiC after activation annealing

Yi-Dan Tang(汤益丹), Xin-Yu Liu(刘新宇), Zheng-Dong Zhou(周正东), Yun Bai(白云), Cheng-Zhan Li(李诚瞻)

Chin. Phys. B . 2019, 28(10): 106101 . **doi:** 10.1088/1674-1056/ab3cc2

Scanning transmission electron microscopy: A review of high angle annular dark field and annular bright field imaging and applications in lithium-ion batteries

Yu-Xin Tong(仝毓昕), Qing-Hua Zhang(张庆华), Lin Gu(谷林)

Chin. Phys. B . 2018, 27(6): 066107 . **doi:** 10.1088/1674-1056/27/6/066107

Two-coupled structural modulations in charge-density-wave state of $SrPt_2As_2$ superconductor

Wang Li, Wang Zhen, Shi Hong-Long, Chen Zhen, Chiang Fu-Kuo, Tian Huan-Fang, Yang Huai-Xin, Fang Ai-Fang, Wang Nan-Lin, Li Jian-Qi

Chin. Phys. B . 2014, 23(8): 086103 . **doi:** 10.1088/1674-1056/23/8/086103

Microstructure evolution of zircaloy-4 during Ne ion irradiation and annealing：An *in situ* TEM investigation

Shen Hua-Hai, Peng Shu-Ming, Zhou Xiao-Song, Sun Kai, Wang Lu-Ming, Zu Xiao-Tao

Chin. Phys. B . 2014, 23(3): 036102 . **doi:** 10.1088/1674-1056/23/3/036102

Misfit-layered compound $PbTiS_3$ with incommensurate modulation：Transmission electron microscopy analysis and transport properties

Shen Xi, Cheng Dan, Zhao Hao-Fei, Yao Yuan, Liu Xiao-Yang, Yu Ri-Cheng

Chin. Phys. B . 2013, 22(11): 116102 . **doi:** 10.1088/1674-1056/22/11/116102

Comparison of cavities and extended defects formed in helium-implanted 6H-SiC at room temperature and 750 °C*

Qing Liao(廖庆)[1], Bingsheng Li(李炳生)[1,†], Long Kang(康龙)[2], and Xiaogang Li(李小刚)[2]

[1] *State Key Laboratory for Environment-friendly Energy Materials, Southwest University of Science and Technology, Mianyang* 621010, *China*

[2] *Institute of Modern Physics, Chinese Academy of Sciences, Lanzhou* 730000, *China*

(Received 12 January 2020; revised manuscript received 7 April 2020; accepted manuscript online 18 April 2020)

The formation of cavities in silicon carbide is vitally useful to "smart-cut" and metal gettering in semiconductor industry. In this study, cavities and extended defects formed in helium (He) ions implanted 6H-SiC at room temperature (RT) and 750 °C followed by annealing at 1500 °C are investigated by a combination of transmission electron microscopy and high-resolution electron microscopy. The observed cavities and extended defects are related to the implantation temperature. Heterogeneously distributed cavities and extended defects are observed in the helium-implanted 6H-SiC at RT, while homogeneously distributed cavities and extended defects are formed after He-implanted 6H-SiC at 750 °C. The possible reasons are discussed.

Keywords: He implantation, cavities, extended defects, transmission electron microscopy, recrystallization

PACS: 61.80.–x, 61.80.Jh, 68.37.Lp, 78.40.Fy **DOI:** 10.1088/1674-1056/ab8abc

1. Introduction

Silicon carbide (SiC), such as 4H-SiC and 6H-SiC, has advanced physical, optical, and electronic properties, such as the high blocking voltage, the low power losses, and the high operational temperatures, therefore 4H-SiC and 6H-SiC can be used in the fields of high-power, high-temperature, and high-frequency.[1–3] In addition, due to the high thermal conductivity, low neutron capture cross-section, high-melting temperature, and mechanical stability, 3C-SiC can be applied to structural components in fusion reactors and advanced fourth-generation fission reactor,[4] *i.e.*, high-temperature gas-cooled reactor as fuel cladding. However, SiC would suffer from intensive neutron irradiation in nuclear irradiation environment. Dense energetic helium (He) atoms can be produced via (n, α) nuclear reaction. He atoms are not stable in interstitial sites in SiC, as a result of very low solubility of He atoms inside SiC. Instead, He atoms are inclined to interact with vacancies to form He–vacancy clusters, such as bubbles.[5] Under high-temperature surroundings, He atoms are escaped from bubbles (outdiffuse from the free surface), leaving cavities inside of SiC. These cavities can deteriorate material mechanical and thermal properties. It is well known that cavities can induce grain-boundaries embrittlement, volume swelling, crack, the decrease in thermal conductivity.[6,7] Therefore, many efforts were paid for improving embrittlement resistance, such as SiC fiber-reinforced SiC (SiC_f/SiC) composites, nanocrystalline SiC. On the contrary, there are some perfect applications of cavities in the semiconductor industry,[8–12] such as fabricating silicon-on-insulator by smart-cut technology, trapping metal impurities, and reducing thread dislocations. Hence, whatever used in semiconductor device fabrication or application in the nuclear power system, the formation and evolution of cavities as functions of implantation fluence, temperature, and thermal treatment conditions are worth investigating.

Among a high number of polytypes, 4H-SiC and 6H-SiC are two of the most important semiconductors due to their wide bandgap and high electron mobility. Consequently, the phenomena of He-implanted 4H-SiC and 6H-SiC are extensively investigated. A rather large number of papers were published in the last three decades on the formation and evolution of He bubbles which show that the formation and growth of the bubble are dependent on the implantation dose, temperature, and annealing conditions.[13–21] However, the influence of as-implanted lattice defects on the evolution of cavities and extended defects in He implanted 6H-SiC is less investigated. Most of the published results are related to the RT implantation and then high-annealing temperature. Nevertheless, there are still some fundamental questions to tb addressed, such as the cavities and defects evolution after elevated implantation temperature and then annealing at high-temperature, and the effect of implantation temperature on morphology and size of cavities in 6H-SiC.

Therefore, this study is aimed at understanding the cavities and defects evolution of He-irradiated 6H-SiC under different implantation temperatures and post-implantation heat treatments. In the present work, a comparison of cavities and

*Project supported by the National Natural Science Foundation of China (Grant No. U1832133) and the Doctor Research Foundation of Southwest University of Science and Technology, China (Grant No. 18zx7141).

†Corresponding author. E-mail: libingshengmvpmvp@163.com

© 2020 Chinese Physical Society and IOP Publishing Ltd

extended defects formed in He-implanted 6H-SiC at RT and 750 °C followed by annealing at 1500 °C was investigated by using cross-sectional transmission electron microscopy (XTEM) and high-resolution TEM (HRTEM). He-implanted 6H-SiC at RT followed by annealing at 1500 °C for 30 min causes a formation of heterogeneous cavities, while the homogeneous cavities were formed in He-implanted 6H-SiC at 750 °C after annealing. Note that the formation of homogeneous cavities is promising for fabricating semiconductor devices which makes the obtained result interesting to use defect engineering to satisfy the special application.

2. Experimental process

In this study, the experimental wafer is oriented $\langle 0001 \rangle_{Si}$ surface with 0.3-mm thickness, n-type 6H-SiC, supplied by MTI Corporation. The size of the sample is 10 mm×10 mm×0.3 mm. The He^{2+} ion implantation with an energy of 300 keV was performed at 320-kV high-voltage platform in the Institute of Modern Physics, Chinese Academy of Sciences. Ion fluence was 1×10^{17} He^{2+}/cm^2 and the two different implantation temperatures were performed, room temperature (RT) and 750 °C. The beam flux during implantation was maintained in the order of 10^{13} ions·cm^{-2}·s^{-1}. In order to provide uniform ion fluence across the sample, the beam was scanned by changing electric field polarity. The size of the beam spot is 16 mm × 17 mm that is larger than the experimental sample. The implantation damage in displacements per atom (dpa) and concentration distribution were simulated by SRIM-2008 quick cascade simulations using the displacement energies of 20 eV for C sublattice and 35 eV for Si sublattice, and the density of 3.21 g/cm^3.[22] Post implantation, the samples were annealed in a tube furnace at 1500 °C for 30 min in a vacuum ($\sim 10^{-1}$ Pa). The microstructures of lattice defects were studied by XTEM and HRTEM using a Tecnai G20 operated at 200 kV with a point resolution of 0.19 nm. Double-tilt sample holder was used in the present experiment. The detailed process of the XTEM sample preparation is reported in Ref. [14]. The HRTEM sample was observed along the [11−20] zone axis. The cavities were observed by changing focused conditions. According to Fresnel contrast, cavities exhibit bright contrast with dark edges under under-focused condition, while exhibit dark contrast with bright edges under over-focused condition. The lattice defects were imaged by bright field (BF) and weak-beam dark field (WBDF). Burgers vectors of the dislocation loops were analyzed using the $\boldsymbol{g} \cdot \boldsymbol{b} = 0$ criterion, where $\boldsymbol{g}$ is the diffraction vector and $\boldsymbol{b}$ is the Burgers vector of the defect. The distribution of cavities was analyzed by using nano measure software.

3. Results and discussion

Figure 1 presents the profiles of the implantation-induced damage and helium atoms percentage in He^{2+} implanted 6H-SiC implanted with 300 keV to a fluence of 1×10^{17} He^{2+}/cm^2, simulated by SRIM 2008. Meanwhile, overviews of the damaged layer exhibited black contrast formed in the He-implanted sample at RT and 750 °C followed by annealing at 1500 °C are also shown in Fig. 1. He implanted 6H-SiC at RT then annealed sample contains a heavily damaged layer which is located at depths ranging from 700 nm to 1250 nm (see Fig. 1(a)). The near-surface region presents a different contrast compared with substrate. this difference is attributed to the formation of an oxide layer. At 750-°C implantation temperature and after annealing, a well-damaged band is located at depths ranging from 1080 nm to 1230 nm. The profiles of implantation-induced damage and He deposition simulated by SRIM 2008 are compared with the damaged layer observed by XTEM. It can be seen that the damaged layer is significantly deeper than the simulated profiles. This is attributed to the volume swelling due to the oxide layer on the surface and the cavities inside the sample.

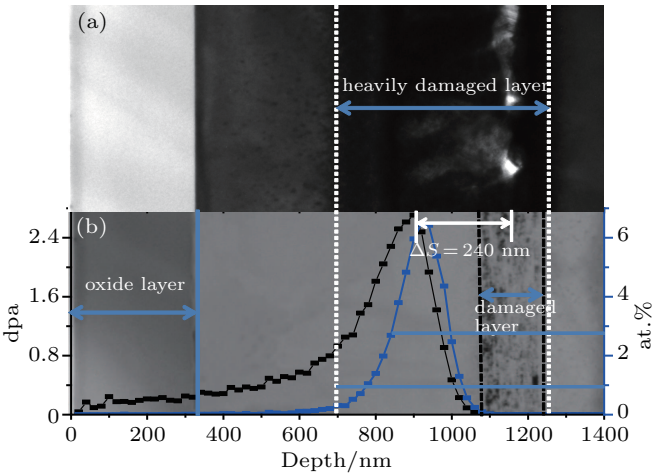


Fig. 1. XTEM bright field micrograph of 6H-SiC implanted with 300-keV He^{2+} ions to a fluence of 1×10^{17} He^{2+}/cm^2 at RT (a) and 750 °C (b) followed by annealing at 1500 °C for 30 min, superposed the distribution of damage and helium deposition of the He-implanted 6H-SiC simulated by SRIM-2008.

Figure 2 presents the bright field cross-sectional transmission electron microscopy with under focused showing the cavity distribution in the damaged layer. For the implantation at RT followed by 1500-°C annealing, there is a cavity layer with 466-nm width, as shown in Fig. 2(a). The observed cavities are distributed heterogeneously. In front of the cavity layer, there are less dense cavities with a small size and at the end of the cavity layer, denser faceted cavities were observed. At peak He deposition, large cavities of near 50-nm diameter were formed. These observed cavities are located at depth of the maximum He deposition. On the other hand, in the middle of the cavity layer, the sizes of observed cavities varied from

2 nm to 34 nm. For the implantation at 750 °C, there is a cavity layer with 155-nm width, as shown in Fig. 2(b), which is significantly lower than that of the implantation at room temperature. Faceted cavities distributed homogeneously were clearly observed, as shown in Fig. 2(c). Meanwhile, the size of the observable cavities is almost uniform. Figure 3 presents the size distribution of observed cavities in the damaged layer for both implantation temperatures. For the implantation at RT, it can be seen that the size of observed cavities ranges from 2 nm to 54 nm and the cavities with less than 10-nm diameter are denser. On the other hand, the cavities size is ranging from 4 nm to 20 nm with most of the observed cavities have approximately 10 nm in diameter in the He-implanted 6H-SiC at 750 °C.

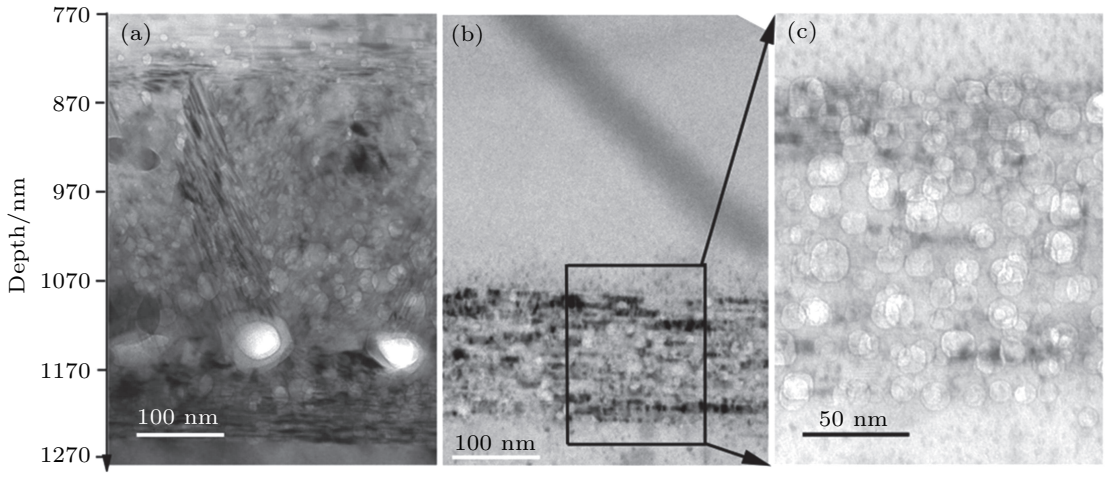


Fig. 2. XTEM bright field with under-focused micrograph showing cavities formed in He-implanted 6H-SiC at (a) RT, (b) and (c) 750 °C, followed by annealing at 1500 °C for 30 min.

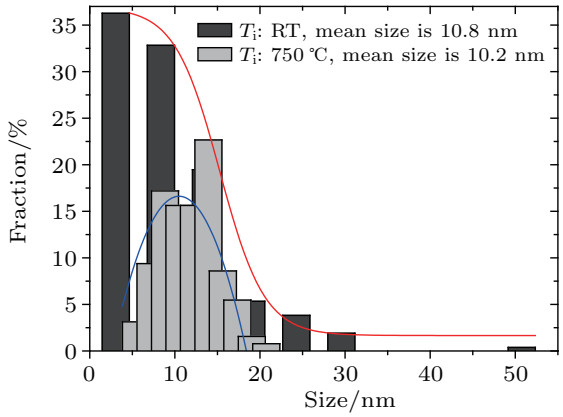


Fig. 3. The size distribution of observed cavities formed in He-implanted 6H-SiC at (a) room temperature, (b) 750 °C, followed by annealing at 1500 °C for 30 min.

Figure 4 presents BF and WBDF images of the damaged layer for the He-implanted 6H-SiC at RT followed by annealing at 1500 °C. The image was viewed along the [11−20] zone axis. Extended defects including dislocation loops, stacking faults and tangled dislocations exhibit black contrasts in BF, but white contrasts in WBDF. The electron diffraction pattern taken from the damaged layer demonstrates 3C-SiC and columnar 6H-SiC formed. In addition, strong streaks and (0001) plane have an intersection angle of approximately 62°. It indicates that columnar 6H-SiC with many stacking faults were formed. The overview of the He-implanted 6H-SiC from the surface to the end of the damaged layer is shown in Fig. 4(a). According to different contrasts, the He^{2+} ions penetrated region can be divided into five different zones, named a1 to a5. At a1 zone, an oxide layer with 340-nm thickness was formed due to a low vacuum ambient of thermal annealing. At a2 zone, some dispersed black-dots were observed, corresponding to interstitial-type point defects. At a3 zone, a heavily damaged layer with dense lattice defects was observed. At a4 zone, it corresponds to the recrystallized layer, containing larger cavities and stacking faults. At a5 zone, it is the same as a3 zone. In order to investigate the types of lattice defects in a2 to a5 zones, WBDF was performed and results are shown in Figs. 4(c) and 4(e). For $\boldsymbol{g} = 0002$, these dispersed black-dots were visible, but were invisible for $g = 1-101$. It indicated these observed black-dots that are Frank loops with a Burgers vector of $b = 1/2\langle 0001\rangle$. At a3 zone, many Frank loops and stacking faults were observed. The size of observed Frank loops ranges from 4 nm to 9 nm. In addition, many stacking faults parallel to sample surface have sizes range from 4 nm to 62 nm. Some stacking faults attached to cavities were clearly observed. At a4 zone, columnar 6H-SiC grains containing many stacking faults were formed. The columnar 6H-SiC grains were connected with larger cavities.

High-resolution TEM images shown in Fig. 5 present the atomic structure of columnar 6H-SiC grains and cavities. It can be seen that facetted cavities with a long axis on the habit plane of stacking faults and a short axis vertical the habit plane of stacking faults. The electron diffraction pattern presents rel-rod streaks that are formed due to dense stacking faults that were formed in columnar 6H-SiC grains. Furthermore, these observed stacking faults belong to interstitial-type, as shown

in Fig. 5(c). Columnar 6H-SiC has two different orientations and their included angle is 48°, as shown in Fig. 5(d). Besides some diffraction spots belong to the as-grown sample, there are ordered diffraction spots attributed to 3C-SiC grains formed in the recrystallized layer. At a5 zone, many tangled dislocations were observed below larger cavities. These tangled dislocation were visible for $\boldsymbol{g} = 1{-}101$ and $\boldsymbol{g} = 0002$. Therefore, these tangled dislocations have a Burgers vector of $b = 1/6[2{-}203]$. Below the tangled dislocations, dense Frank loops were observed. For $\boldsymbol{g} = 1{-}101$, many stacking faults were observed in the zone that contains many tangled dislocation. For the He-implanted 6H-SiC at 750 °C followed by annealing at 1500 °C. Lattice defects are almost homogeneously distributed in the damaged layer, as shown in Fig. 6. For $\boldsymbol{g} = 000{-}2$, many Frank loops with sizes ranging from 3 nm to 9 nm were observed, as shown in Figs. 6(a) and 6(b). Furthermore, some Frank loops were observed at both sides of the damaged layer. For $\boldsymbol{g} = 1{-}101$, many stacking faults parallel to the sample surface with sizes ranging from 4 nm to 38 nm were observed, as shown in Figs. 6(c) and 6(d). No stacking faults were observed outside the damaged layer.

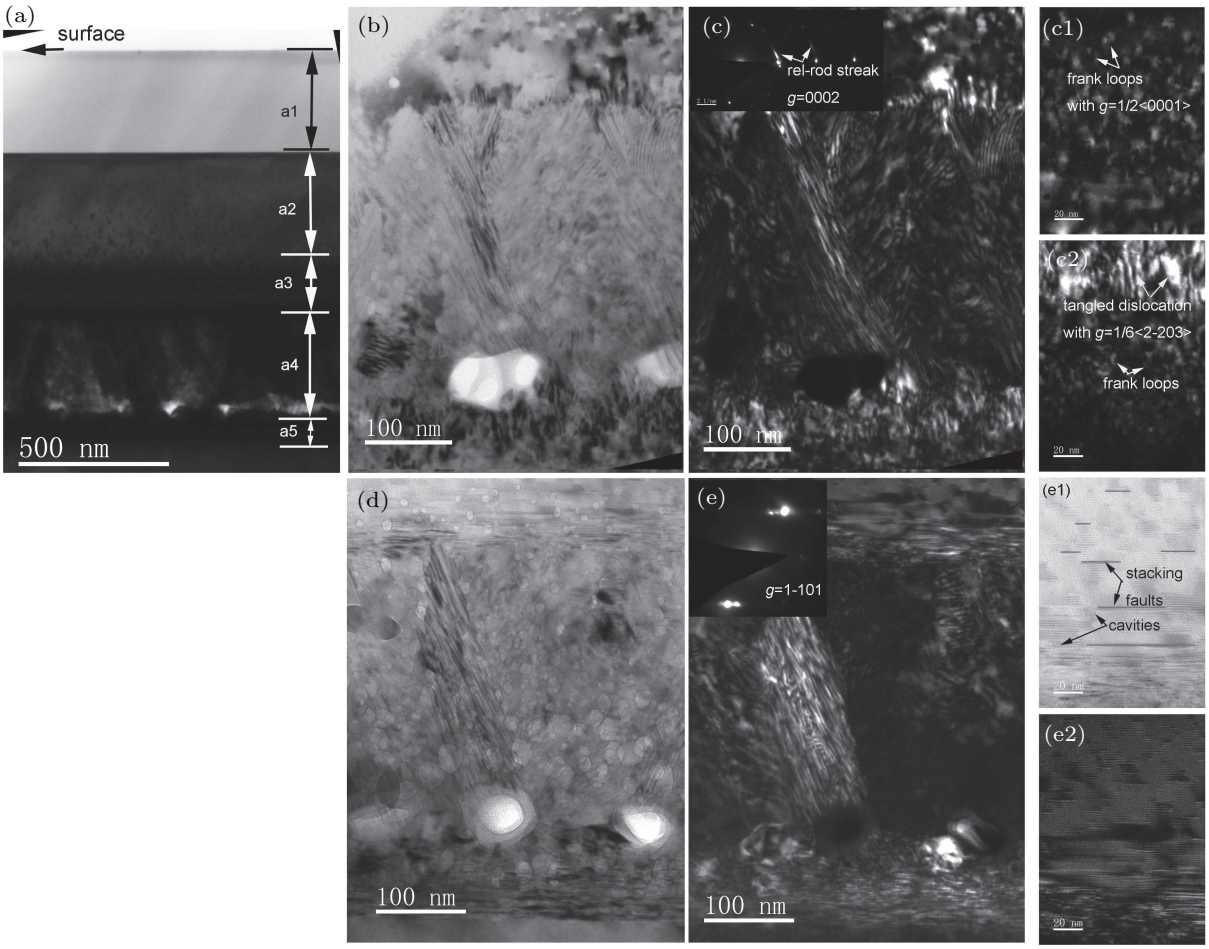


Fig. 4. XTEM micrographs showing the extended defects formed in He-implanted 6H-SiC at RT followed by annealing at 1500 °C for 30 min, (a) an overview of the damaged layer divided by five different zones, (b) bright-field and (c) weak-beam dark field with $\boldsymbol{g} = 0002$ showing Frank loops, (c1) and (c2) showing more detail of Frank loops, (d) bright-field and (e) weak-beam dark field with $\boldsymbol{g} = 1\bar{1}01$ showing stacking faults, (e1) and (e2) showing more details of stacking faults.

For the implantation at RT followed by annealing at 1500 °C, the distributions of extended defects and cavities are related to the nuclear atomic displacement distribution and the helium deposition simulated by SRIM. The distributions of observed extended defects and cavities are heterogeneous. Some reasons can account for the present experimental results. For He-implanted 6H-SiC at RT, it is easy to induce an amorphous layer when the irradiation dose is up to 0.3 dpa.[13] In the amorphous layer, tiny bubbles with near 1 nm in diameter are formed at the location of the maximum He deposition. At both sides of the amorphous layer, there are crystalline layers containing many lattice defects. According to the profile of the nuclear atomic displacement distribution simulated by SRTM, it can form an amorphous layer with over 500-nm width. After annealing at 1500 °C, recrystallization occurs. Columnar 6H-SiC containing many stacking faults and 3C-SiC grains are formed in the recrystallized layer. The mechanism of the recrystallization process have been inves-

tigated by many researchers.[13,23–26] Complete recrystallization of amorphous 6H-SiC formed by He implantation occurs at temperatures between 800 and 900 °C. It is easy to form columnar 6H-SiC, independent of ion species. It should be noted that columnar 6H-SiC grains are only formed in ion-implanted 6H-SiC oriented ⟨0001⟩ surface. We do not observe columnar 6H-SiC grains formed after recrystallization of 6H-SiC with other orientations. The present experimental result shows that columnar 6H-SiC starts at larger cavities, where corresponds to the maximum He deposition. In Si- or Ge-implanted 6H-SiC, columnar 6H-SiC grains are also formed at the maximum ion deposition.[25,26] Therefore, it is reasonable to regard that impurity atoms introduced by ion implantation could lead to columnar growth. A fast increase in the size of bubbles occurs after annealing. Due to very low permeability of He atoms in SiC, some He atoms can escape from bubbles to form cavities after annealing. Oliviero *et al.*[27] investigated a thermal He desorption in He-implanted 6H-SiC, and found a desorption peak at 1200 K, corresponding to He emission from He–vacancy clusters. The tiny bubbles coalesce into large cavities through vacancy absorption and interstitial emission. These interstitials are easy to agglomerate on the (0001) plane to form Frank loops with $\boldsymbol{b} = 1/2\langle 0001\rangle$. Frank loops can act as sinks for interstitials to increase in the size of Frank loops. Subsequently, the strain of Frank loops can promote the emission of Shockley partial dislocations in the (0001) plane.[23] Extended stacking faults are formed between Shockley partial dislocations. Figures 3(d1) and 3(d2) clearly show some stacking faults attached by cavities. Interstitials easily migrate towards the sample surface compared with the vacancies. This is due to sample surface acting as sinks for lattice defects. Therefore, it can be seen that many Frank loops were formed at a2 zone. According to the migration energy of C and Si vacancies (V_C is 4.1 eV and V_{Si} is 2.35 eV),[28] C and Si vacancies are very mobile to coalesce into large vacancy clusters during annealing at 1500 °C. Shen *et al.*[18] observed in He-implanted 6H-SiC, a rapid increase in the bubble size after annealing at 1200 °C. The vacancy migration is affected by impurities and extended defects. For example, vacancy migration is retarded by trapping He atoms, while vacancy migration is enhanced via stacking faults,[29] so it can be seen a facetted cavity with a long axis on the habit plane of stacking faults, as shown in Fig. 5(c). We recently found the nucleation and growth of cavities on stacking faults are preferential in He-irradiated 3C-SiC at 1000 °C.[30] The formation of tangled dislocations is due to the fast growth of Frank loops. More importantly, defect annealing is not significant during implantation at RT, many implantation-induced Frenkel pairs are stable during He implantation. Due to the profile of the nuclear atomic displacement distribution exhibiting a Bragg peak, the implantation-induced lattice defects and He deposition are different as a function of He penetration depth. The nucleation and growth of cavities are more evident in the region of the maximum He deposition than other regions.

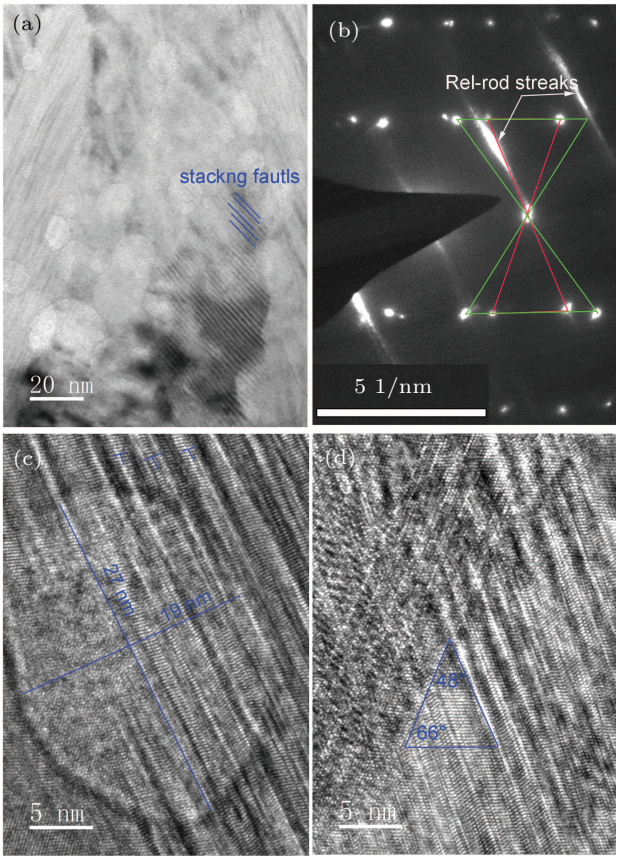


Fig. 5. HRTEM micrographs showing recrystallization layer containing (a) stacking faults, (b) selected-area electron diffraction pattern showing rel-rod streaks due to stacking faults and additional diffraction spots due to 3C-SiC grains, (c) one facetted cavity preferential growth on the stacking faults, (d) two different orientations of columnar 6H-SiC with included angle of 48°. The HRTEM micrograph of (a) was taken from the depth of about 1000 nm to 1160 nm.

For the He-implantation at 750 °C followed by annealing at 1500 °C, dynamic annealing is evident due to the increase in the recombination rate of Frenkel pairs at elevated temperature; many implantation-induced Frenkel pairs are recovered during He implantation at 750 °C. The residual defects were decreased in the as-implanted sample. After thermal annealing, these residual defects easily migrated and recovered compared to stable defect clusters formed in the RT implantation. Therefore, the width of the damaged layer is significantly lower than that of implantation at RT. According to previous results of He-implanted 6H-SiC, the distribution of the damaged layer can be well simulated by SRIM program. It is generally regarded that the maximum He deposition is located in the middle of the damaged layer. According to the profile of He deposition and location of the damaged layer, it can get that the threshold He concentration for the formation

of cavities is 2.8 at.% during He implantation at 750 °C. It is consistent with the report of Zhang *et al.*[16] which shows that the threshold dose for forming cavities increases with increasing implantation temperature, because the concentration of stable vacancies is reduced at elevated temperature. The formation of He bubbles relays on the concentration of vacancies. No amorphous layer is formed in the damaged layer, resulting in no columnar 6H-SiC containing stacking faults effect on the growth of cavities. Furthermore, the implantation-induced lattice defects do not have a larger deviation with penetration depth as compared with the case of implantation at RT. The nucleation and growth of cavities are almost homogeneous in a range of short distance. It can be speculated that homogeneous cavities would be formed in He-implanted 6H-SiC at elevated temperature, where no amorphous layer is formed. Frank loops and stacking faults are formed through the growth of cavities which cause homogeneous extended defects distribution.

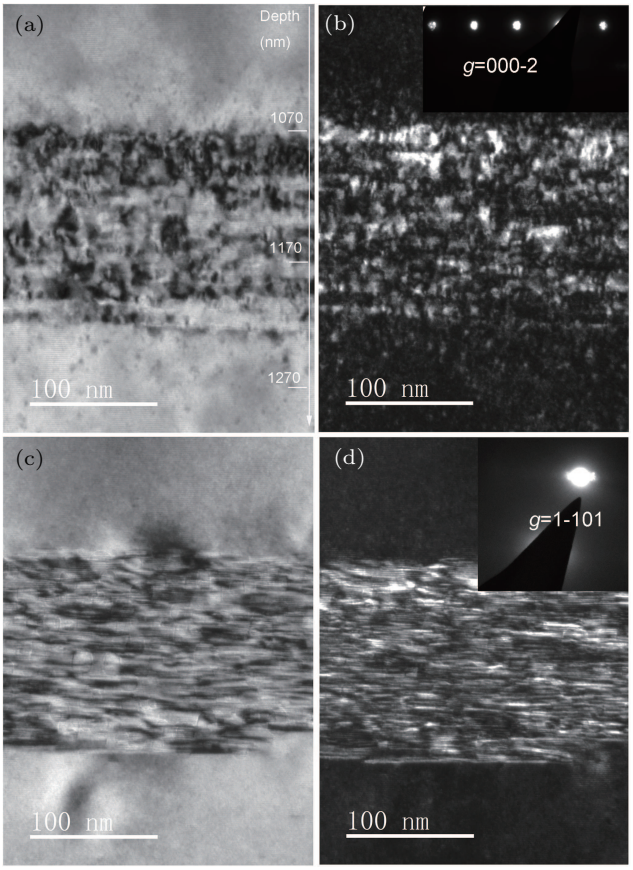


Fig. 6. XTEM micrographs showing the extended defects formed in He-implanted 6H-SiC at 750 °C followed by annealing at 1500 °C for 30 min, (a) bright-field and (b) weak-beam dark field with $\boldsymbol{g} = 000\bar{2}$ showing Frank loops, (c) bright-field and (d) weak-beam dark field with $\boldsymbol{g} = 1101$ showing stacking faults. The diffraction vector was shown in inset of the corresponding figure.

4. Conclusions

In the present study, 6H-SiC was implanted with He^{2+} ions at RT and 750 °C followed by annealing at 1500 °C for 30 min. The microstructure evolution were investigated by XTEM and HRTEM. The main results are summaries as follows.

For the implantation at RT followed by annealing at 1500 °C, cavities and extended defects are formed and distributed heterogeneously. At He peak deposition, the facetted cavities have the largest sizes over 30 nm. Stacking faults can enhance cavity growth. Interstitials are fast mobile towards to the sample surface during annealing at 1500 °C. Subsequently, some interstitials migrate and agglomerate into defect clusters, resulting in Frank loops. The strain of Frank loops can promote the emission of Shockley partial dislocations in the (0001) plane, forming stacking faults.

For the implantation at 750 °C followed by annealing at 1500 °C, cavities and extended defects are formed and distributed homogeneously with 10 nm of average diameter. The observable damaged layer is significantly less than that at RT implantation. The threshold He concentration for the formation of cavities is 2.8 at.% during He implantation at 750 °C.

The main reason for the formation of heterogeneous cavities after implantation at RT is due to the formation of the amorphous layer. After annealing at 1500 °C, recrystallization introduces columnar 6H-SiC with dense stacking faults in the damaged layer. The growth of cavities is fast on the stacking faults, resulting in heterogeneous cavities. Therefore, homogeneous cavities would be formed in 6H-SiC He-implanted at elevated temperature, where no amorphous layer is formed. The research is valuable for defect engineering of cavities trapping metal impurities and a decrease in transient enhanced diffusion of ion doping in the semiconductor industry.

References

[1] Wesch W 1996 *Nucl. Instrum. Methods Phys. Res. B* **116** 305
[2] Wang K, Doerner R P, Baldwin M J and Parish C M 2018 *J. Nucl. Mater.* **509** 679
[3] Qian G, Lei W S, Niffenegger M and Gonzalez V F 2018 *Philos. Mag.* **98** 959
[4] Katoh Y, Snead L L, Szlufarska I and Weber W J 2012 *Curr. Opin. Solid State Mater. Sci.* **16** 143
[5] Sun J J, Li B S, You Y W, Hou J, Xu Y C, Liu C S, Fang Q F and Wang Z G 2018 *J. Nucl. Mater.* **503** 271
[6] Snead L L, Nozawa T, Katoh Y, Byun T S, Kondo S and Petti D A 2007 *J. Nucl. Mater.* **371** 329
[7] Chen J, Jung P and Ullmaier H 2005 *J. Nucl. Mater.* **336** 194
[8] Daghbouj N, Li B S, Karlik M and Declemy A 2019 *Appl. Surf. Sci.* **466** 141
[9] Li B S, Wang Z G, Wei K F, Shen T L, Yao C F, Zhang H P, Lu X R and Han W T 2019 *Fusion Eng.* **142** 6
[10] Alquier D, Bongiorno C, Roccaforte F and Raineri V 2005 *Appl. Phys. Lett.* **86** 211911
[11] Cherkashin, Daghbouj N, Seine G, Claverie A 2018 *J. Appl. Phys.* **123** 161556
[12] Daghbouj N, Cherkashin N, Darras F X, Paillard V, Fnaiech M, Claverie A 2016 *J. Appl. Phys.* **119** 135308
[13] Li B S, Du Y Y and Wang Z G 2015 *Nucl. Instrum. Methods Phys. Res. B* **345** 53
[14] Li B S, Liu H P, Xu L J, Wang J, Song J, Peng D P, Li J H, Zhao F Q, Kang L, Zhang T M, Tang H X and Xiong An L 2020 *Appl. Surf. Sci.* **499** 143911

[15] Liu Y Z, Li B S and Zhang L 2017 *Chin. Phys. Lett.* **34** 052801
[16] Zhang C H, Donnelly S E, Vishnyakov V M and Evans J H 2003 *J. Appl. Phys.* **94** 6017
[17] Chen J, Jung P and Trinkaus H 2000 *Phys. Rev. B* **61** 12923
[18] Shen Q, Zhou W, Ran G, Li R X, Feng Q J and Li N 2017 *Materials* **10** 101
[19] Han W T and Li B S 2018 *J. Nucl. Mater.* **504** 161
[20] Daghbouj N, Li B S, Callisti M, Sen H S, Karlik M and Polcar T 2019 *Acta Mater.* **181** 160
[21] Dahbouj N, Li B S, Callisti M, Sen H S, Lin J, Ou X, Karlik M, Tolcar T 2020 *Acta Mater.* **188** 609
[22] Ziegler J F, Ziegler M D and Biersack J P 2010 *Nucl. Instr. Method B* **268** 1818
[23] Bae In-Tae, Ishimaru M, Hirotsu Y and Sickafus K E 2004 *J. Appl. Phys.* **96** 1451
[24] Gao F, Devanathan R, Zhang Y, Posselt M and Weber W J 2006 *J. Mater. Res.* **21** 1420
[25] Harada S, Ishimaru M, Motooka T, Nakata T, Yoneda T and Inoue M 1996 *Appl. Phys. Lett.* **69** 3534
[26] Heera V, Kogler R, Skorupa W and Stoemenos J 1995 *Appl. Phys. Lett.* **67** 1999
[27] Oliviero E, Beaufort M F and Barbot J F 2003 *J. Appl. Phys.* **93** 231
[28] Gao F, Weber W J, Posselt M and Belko V 2004 *Phy. Rev. B* **69** 245205
[29] Xi J Q, Liu B, Yuan F L, Zhang Y W and Weber W J 2017 *Scr. Mater.* **139** 1
[30] Li B S, Liu H P, Shen T L, Xu L J, Wang J, Zhao F Q, Peng D P, Li J H, Sheng Y B and Xiong A L 2020 *J. Eur. Cera. Soc.* **40** 1014